Glycosylated IgG antibodies contribute to the recovery of haemorrhagic fever with renal syndrome patients

Chuansong Quan[1,2,3†], Lu Wang[3,4†], Jiming Gao[5†], Yaoni Li[6†], Xiaoyu Xu[7†], Houqiang Li[3], Zixuan Gao[7], Wenxu Ruan[7], Hongzhi Liu[3], Qian Li[3], Weijia Xing[3], Liqiong Zhao[6], Michael J. Carr[8,9], Weifeng Shi[10,11*], Haifeng Hou[3*]

[1]Key Laboratory of Emerging Infectious Diseases in Universities of Shandong, Shandong First Medical University & Shandong Academy of Medical Sciences, Ji'nan, 250117, China

[2]The Second Affiliated Hospital of Shandong First Medical University, Taian, 271000, China

[3]School of Public Health, Shandong First Medical University & Shandong Academy of Medical Sciences, Ji'nan, 250117, China

[4]Medical Records and Statistics Management Office, Tengzhou Central People's Hospital, Zaozhuang, 277500, China

[5]Department of Neurobiology and Physiology, School of Clinical and Basic Medicine, Shandong First Medical University& Shandong Academy of Medical Sciences, Ji'nan, 250117, China

[6]Baoji Central Hospital, Baoji, 721008, China

[7]School of Life Sciences, Shandong First Medical University & Shandong Academy of Medical Sciences, Taian, 271016, China.

[8]National Virus Reference Laboratory, School of Medicine, University College Dublin, D04 E1W1, Ireland.

[9]International Collaboration Unit, International Institute for Zoonosis Control, Hokkaido University, N20 W10 Kita-ku, Sapporo 001-0020, Japan.

[10]Ruijin Hospital, Shanghai Jiao Tong University School of Medicine, Shanghai, 200025, China.

[11]Shanghai Institute of Virology, Shanghai Jiao Tong University School of Medicine, Shanghai, 200025, China

*Correspondence:

Haifeng Hou: hfhou@sdfmu.edu.cn

Weifeng Shi: shiwf@ioz.ac.cn

†These authors contributed equally to this work

Abstract

Haemorrhagic fever with renal syndrome (HFRS) is a fatal disease caused by Hantaan virus (HTNV) infection. Humoral immunity is essential for effective viral clearance, however, the glycosylation characteristics of immunoglobulin G (IgG) in HFRS patients is not well known. Peripheral blood mononuclear cells from HFRS patients were obtained for B subset analysis using scRNA-seq and flow cytometry. HTNV specific IgG antibody titers were detected by enzyme-linked immunosorbent assay, and IgG glycosylation was analyzed by ultra-performance liquid chromatography. The proportions of the antibody-secreting memory (ASM) B cells and plasmablasts (PB) were significantly expanded among acute HFRS patients. We discovered significantly increased fucosylated IgG and decreased bisecting N-acetylglucosamine during the convalescent phase of HTNV infection. Meanwhile, positive correlations were observed between ASM subsets and galactosylation/sialylation in the IgG Fc region, and between PB subsets and sialylation. Notably, the glycosylation-related genes, such as *RPN1 and RPN2*, were primarily expressed differentially in the ASM and PB subclusters which were enriched in the N-glycosylation modifications of proteins through asparagine. Our findings indicated that IgG N-glycosylation may play a crucial role in combating HTNV infection and contributing to clinical recovery, which provided new insights for optimizing glycoengineered therapeutic antibodies.

Keywords: Haemorrhagic fever with renal syndrome (HFRS); Hantaan virus (HTNV); B cell; Immunoglobulin G (IgG); Glycosylation; Inflammation

Introduction

The causative agent of haemorrhagic fever with renal syndrome (HFRS) is Hantaan virus, which belongs to the family *Hantaviridae* and is primarily transmitted by rodents (Zheng et al., 2019). China is the most heavily affected country by HFRS, accounting for >90% of global cases, and a total of 32,462 cases of HFRS were reported in China during 2019–2022, with a fatality rate ranging from 0.1 to 15% (R. Li et al., 2023) (https://www.chinacdc.cn).

Hantaviruses are tri-segmented, single-stranded, negative-sense RNA viruses, whose genomes consist of three regions: large (L), medium (M), and small (S). The glycoproteins Gn and Gc, encoded by the M segment, can infect target cells - primarily vascular endothelial cells - via β3 integrin receptors (Pizarro et al., 2019). Simultaneously, they could also infect other cell types, such as mononuclear macrophages and dendritic cells, leading to systemic viral infection. Although hantavirus replication is thought to occur primarily in the vascular endothelium without direct cytopathic effects, a plethora of innate immune cells mediate host antiviral defenses. These include natural killer cells, neutrophils, monocytes, and macrophages, together with pattern recognition receptors (PRRs), interferons (IFNs), antiviral proteins, and complement activation, e.g., via the pentraxin 3 (PTX3) pathway, which can exacerbate HFRS disease progression leading to immunopathological damage through cytokine/chemokine production, cytoskeletal rearrangements in endothelial cells, ultimately amplifying vascular dysfunction (Tariq & Kim, 2022). Rapid and effective humoral immune responses, however, such as neutralizing antibody responses targeting the glycoproteins Gn/Gc, contribute to rapid recovery from HFRS and are critical for protection from severe disease (Engdahl & Crowe, 2020; Li et al., 2020).

83 Immunoglobulin G (IgG) N-linked glycosylation mediates critical functions
84 modulating antiviral immunity during viral infection. Changes in the conserved
85 N-linked glycan Asn297 in the Fc region of IgG typically by fucosylation,
86 galactosylation, or sialylation can alter antibody effector function. A reduction in core
87 fucosylation decreases IgG binding to NK cell FcγRIIIa promotes antibody-dependent
88 cellular cytotoxicity (ADCC) necessary for clearance of viruses, including
89 SARS-CoV-2, dengue and HIV-1 whereas sialylation can attenuate immune responses
90 resulting in immune evasion (Ash et al., 2022; Haslund-Gourley et al., 2024; Hou et
91 al., 2021; Wang et al., 2017). Changes in IgG and other protein N-linked
92 glycosylation profiles therefore shape virus-host interactions and disease progression.
93 Importantly, there have not been prior studies specifically examining plasma IgG
94 N-glycome profiles derived from chromatographic peak data in HFRS patients,
95 particularly in relation to seroconversion status. This gap in our knowledge motivated
96 our systematic investigation of both total and virus-specific IgG glycosylation
97 dynamics during acute infection. In the present study, we combined scRNA-seq and
98 flow cytometry to reveal the phenotypes of B cell responses during Hantaan virus
99 (HTNV) infection, and explored the transcriptomic features of reactive B cell subsets.
100 A total of 166 HFRS patients, including 65 paired HFRS samples, were employed to
101 profile the IgG-Fc glycosylation pattern and to investigate the potential regulatory
102 role of IgG-Fc glycosylation in HFRS pathogenesis.

103 **Results**

104 **B cell compositional characteristics in HFRS patients**

105 To characterize the humoral immune profiles in HFRS patients, we enrolled 166
106 suspected HTNV-infected patients who were admitted to Baoji Central Hospital in
107 Shaanxi Province, China, between October 2019 and January 2022. Among them, 65

108 met the inclusion criteria and were included in the study (Figure 1). We identified a
109 total of eight cell subpopulations, including subsets of CD4 T cells, CD8 T cells,
110 CD14 monocytes, NK cells, B cells, platelets, endothelial progenitor cells, and red
111 blood cells (Figure 2—figure supplement 1A and B). The proportions of these cell
112 types were comparable between acute HFRS patients and healthy controls, with no
113 significant batch effects observed (Figure 2—figure supplement 1C). CD4 T cells
114 (31.4%) were the predominant subset prior to HTNV infection, whereas CD8 T cells
115 (44%) became the dominant population post-infection. Notably, the proportions of
116 NK cells (15.9% to 5.6%, $p<0.001$) and platelets (3.1% to 0.6%, $p<0.01$) significantly
117 decreased, whereas the level of CD14 monocytes (15.9% to 32.3%, $p<0.05$) nearly
118 doubled. The overall proportions of B cells, however, did not exhibit significant
119 changes (Figure 2—figure supplement 1D and E).

120 To precisely elucidate the role of B cell subsets in anti-HTNV infection, we
121 classified B cells into eight subsets, including antibody-secreting memory B cells
122 (ASM), double-negative B cells (DN), intermediate memory B cells (IM), marginal
123 zone-like B cells (MZB), naive B cells (naive B), plasmablasts (PB), quiescent resting
124 memory B cells (RM), and exhausted tissue-like memory B cells (TLM) (Figure 2A
125 and B, and Figure 2—figure supplement 1F). We discovered that significant
126 expansion of ASM, PB, and RM cell populations in acute HFRS patients compared to
127 healthy controls, accompanied by contraction of DN, IM, and naive B cell
128 compartments post-infection (Figure 2C). In healthy controls, naive B cells (42.87%),
129 DN B cells (26.65%), and TLM B cells (16.13%) constituted the majority of the B
130 cell population. However, ASM (30.96%), PB cells (11.12%) and RM B cells (2.88%),
131 became the dominant subsets after HTNV infection (Figure 2D and Supplementary
132 file 1).

133 To validate the accuracy of our single-cell subpopulation analysis, we employed
134 flow cytometry to quantify the B cell subsets in acute and convalescent HFRS patients
135 (Figure 2E). The results demonstrated that ASM (39.48% vs. 24.57%, $p<0.001$) and
136 PB (23.97% vs. 2.61%, $p <0.001$) subsets were significantly amplified in the acute
137 phase compared to the convalescent phase (Figure 2F). Conversely, the number of
138 naive B cells (32.78% vs. 48.92%, $p=0.003$) and CSM cells (18.65% vs. 27.15%,
139 $p=0.008$) recovered rapidly in the convalescent stage (Figure 2F), consistent with the
140 observations at the transcriptome level. No significant differences were observed for
141 other B cell subtypes between the acute and convalescent stages (Figure 2—figure
142 supplement 2). These results demonstrated that several B cell subpopulations were
143 effectively activated following HTNV infection.

144 **Dynamic characteristics of the IgG N-glycome in HFRS patients**

145 HFRS patients were further stratified into three age groups (≤44, 45-59, and ≥60
146 years). IgG glycosylation was analyzed by ultra-performance liquid chromatography.
147 As shown in Supplementary file 2, no significant differences in IgG glycosylation
148 were observed between age groups, except for galactosylation ($p=0.001$). Similarly,
149 no sex-based differences in IgG-Fc glycosylation were noted (Supplementary file 3).
150 However, the levels of IgG with bisecting GlcNAc (15.72% vs. 14.51%, $p<0.001$),
151 galactosylated IgG (74.26% vs. 71.15%, $p<0.001$), and sialylated IgG (22.44% vs.
152 21.62%, $p<0.001$) were significantly higher in the acute phase compared to the
153 convalescent phase. Conversely, fucosylated IgG levels (94.29% vs. 94.89%, $p<0.001$)
154 were lower in the acute phase (Supplementary file 4), indicating that IgG
155 N-glycosylation plays a critical role in the anti-infection process. Multivariate linear
156 regression was employed to mitigate potential confounding by genetic and
157 environmental factors in the glycomics analysis. While no significant associations

158 were observed for most glycan models (fucosylation, p=0.526; bisecting GlcNAc,
159 p=0.069; and sialylation, p=0.058), we discovered sex showed a potentially influential
160 effect on galactosylation (p=0.001) (Supplementary files 5-8). These results suggest
161 that while most glycan features appear unaffected by the examined covariates,
162 galactosylation may be subject to sex-specific biological regulation.

163 Among the 130 paired blood samples from 65 patients, 38 (29.2%) were negative
164 for HTNV nucleocapsid protein-specific IgG antibodies, and 92 (70.8%) were
165 seropositive. For the 24 patients with both seronegative and seropositive samples,
166 levels of bisecting GlcNAc (16.16% vs. 14.54%, p<0.001), galactosylation (74.12%
167 vs. 70.94%, p=0.006), and sialylation (22.92% vs. 21.80%, p=0.008) were higher in
168 the seronegative period, whereas that of fucosylation was lower (94.36% vs. 94.74%,
169 p= 0.024) in this period (Figure 3A). Notably, bisecting GlcNAc and sialylated IgG
170 levels decreased as HTNV nucleocapsid protein (NP)-specific antibody titers
171 increased (Figure 3B), highlighting a potential link between antibody levels and
172 IgG-Fc glycosylation.

173 **The IgG N-glycome in HFRS patients with seroconversion**

174 A four-fold or greater increase in HTNV NP-specific antibody titers usually
175 indicates a protective humoral immune response during the acute phase
176 (Onwuchekwa et al., 2023). We observed a significant increase in the Fc fucosylation
177 (94.18% vs. 94.48%, p=0.044) and a decrease in bisecting GlcNAc (16.41% vs.
178 14.71%, p=0.001) post the four-fold antibody titer increase compared to the baseline.
179 However, no significant differences were observed in galactosylation and sialylation
180 (Figure 3C), suggesting that fucosylation and bisecting GlcNAc may play key roles in
181 anti-HTNV infection and recovery.

182 **The potential source of the IgG N-glycome during HTNV infection**

183 Positive correlations were observed between the ASM subsets and both
184 galactosylation (p=0.017, r_s=0.418) and sialylation (p=0.008, r_s=0.458) in the
185 antibody Fc region, as well as between the PB subsets and sialylation (p=0.036,
186 r_s=0.372) (Figure 4A-C). Therefore, we speculated that galactosylated antibodies may
187 primarily originate from the ASM subsets, while sialylated antibodies may derive
188 from the ASM and PB subsets.

189 To investigate the process of glycosylated antibody production secreted by the
190 ASM and PB subsets, we identified differentially expressed genes (DEGs) among the
191 eight B cell subpopulations. Notably, the most DEGs were observed in the ASM (470),
192 naive (312), and TLM (333) B subpopulations, respectively (Figure 4—figure
193 supplement 1A and Supplementary file 9). Specifically, among all the upregulated
194 genes, the expressions of glycosylation-related, mitochondrial respiratory-related, and
195 peptide chain elongation-related genes among the ASM, PB, and RM populations
196 were elevated after HTNV infection, including *RPN2*, *MT-ND6*, and *RPS26* (Figure
197 4—figure supplement 1B and Supplementary file 10). On the contrary, the
198 upregulated genes in the naive, DN, and IM populations were related to
199 anti-inflammatory and immunosuppressive effects, inhibition of the antioxidative
200 function, response to environmental stress, and B-cell growth and development, such
201 as *TSC22D3*, *TXNIP*, *DUSP1*, and *KLF6*, whereas the downregulated genes played an
202 important role in the inflammatory response, cell motility, and antigen presentation,
203 including *LTB*, *ACTG1*, and *HLA-DRB5* (Figure 4—figure supplement 1C and
204 Supplementary file 11).

205 Unexpectedly, we observed significant changes in the expression of
206 glycosylation-related genes (GRGs) in the ASM, PB, and RM subclusters during
207 HTNV infection compared to healthy controls. *RPN1* and *RPN2* were prominently

208 upregulated, which encoded subunits of the oligosaccharyltransferase complex
209 (Figure 4D). This implied that the process of glycosylation during HTNV infection
210 was rapidly activated among the ASM and PB subclusters. In the ASM subcluster, the
211 fold change of GRGs from all four glycosylation modification-related genes, aside
212 from *RPN1* and *RPN2*, was similar, suggesting that ASM may undergo complex and
213 diverse glycosylation modification processes.

214 To enhance our understanding of the transcriptomic characteristics of
215 GRG-high-expressing PB and ASM subclusters, we conducted a comprehensive
216 pathway enrichment analysis and identified significant enrichment of pathways
217 related to glycosylation modifications, including the endoplasmic reticulum
218 protein-containing complex, rough endoplasmic reticulum, and protein N-linked
219 glycosylation via asparagine (Figure 4E). Additionally, gene sets associated with
220 glycosylation modifications showed positive regulation of these pathways (p=0.002,
221 Figure 4F). These results indicated that glycosylation modifications in the ASM, PB,
222 and RM subpopulations were dynamically regulated during the acute phase of HFRS,
223 likely to satisfy the amplified anti-HTNV antibody requirement and accelerate viral
224 clearance.

225 **Discussion**

226 IgG glycosylation is a key regulator of inflammatory responses for infectious
227 diseases, acting as a molecular switch between anti-inflammatory and
228 pro-inflammatory effects upon antigenic challenge. One of the most significant
229 findings of the present study is the elevation in IgG fucosylation and reduction in
230 bisecting GlcNAc levels at the time of a four-fold increases in the HTNV NP-specific
231 antibody titers. Afucosylation is known to enhance antibody-dependent cellular
232 cytotoxicity (ADCC) by increasing the affinity of IgG-Fc for the FcγRIIIa receptor on

233 NK cells, leading to heightened production of inflammatory cytokines such as IL-1β,
234 IL-6, IFN-γ, and TNF-α (Larsen et al., 2021; Lu, Suscovich, Fortune, & Alter, 2018;
235 Wieczorek, Braicu, Oliveira-Ferrer, Sehouli, & Blanchard, 2020). Increase in
236 bisecting GlcNAc linked to Fc induces enhanced affinity for the FcγIIIa receptor and
237 enhanced ADCC function of the antibodies (Giron et al., 2020; Hou et al., 2021;
238 Irvine & Alter, 2020). However, rather than directly influencing the Fc receptor
239 binding, this modification enhances antibody functionality through afucosylation,
240 which subsequently increases the binding affinity to the FcgRIIIa receptor (Ackerman
241 et al., 2018; Jennewein & Alter, 2017). Our findings provide evidence that the
242 dynamic alterations in glycosylation patterns, characterized by increased fucosylation
243 and decreased bisecting GlcNAc levels during viral infection, are involved in disease
244 pathogenesis and clinical recovery, suggesting their dual utility as both diagnostic
245 biomarkers and promising therapeutic targets.

246 We also observed elevated galactosylation levels in the acute phase compared to the
247 convalescent phase, a phenomenon also reported in SARS-CoV-2 infections but not in
248 chronic diseases and cancers (Hou et al., 2021; Liu et al., 2018). Increased
249 galactosylation may expand the distance between CH2 domains, exposing key amino
250 acids for FcγRIIIa binding and enhancing ADCC functions (Houde, Peng, Berkowitz,
251 & Engen, 2010). Simultaneously, the increase in the ASM subset, which positively
252 correlated with galactosylation, may reflect polyclonal activation of memory B cells
253 driven by pattern recognition receptors and cytokines, leading to the production of
254 galactosylated antibodies. Similarly, sialylation levels were higher in the acute
255 patients, potentially linked to the expansion of the ASM and PB subsets. In this study,
256 the PB subset was significantly elevated in the acute phase and positively correlated
257 with sialylation, suggesting that rapidly proliferating plasmablasts may contribute to

258 the secretion of sialylated antibodies; however, the mechanisms behind this require
259 further investigation.

260 Antibody-related glycogenes are significantly activated following Hantaan virus
261 infection. We noted that ribophorin I and II (RPN1 and RPN2) were significantly
262 upregulated in the ASM/IM/PB/RM subsets after Hantaan virus infection, which
263 linked the high mannose oligosaccharides with asparagine residues found in the
264 Asn-X-Ser/Thr consensus motif (Hwang et al., 2025). We speculate that they
265 continuously attach the synthesized glycan chains to the constant region of antibodies
266 during antibody synthesis. Similarly, fucosyltransferase 8 (FUT8) in the ASM subset,
267 catalyzing the alpha1-2, alpha1-3, and alpha1-4 fucose addition (Wang & Ravetch,
268 2019; Yang et al., 2015), was downregulated in the mRNA translation, and the levels
269 of fucosylated antibodies were naturally lower in the acute HFRS patients. Meanwhile,
270 the beta-1,4-galactosyltransferase (beta4GalT) gene expression was significantly
271 elevated in the ASM subpopulation during the acute phase, which also correlated with
272 increased levels of galactosylated antibodies in serum (Wang & Ravetch, 2019).
273 However, we did not observe significant upward changes in sialyltransferase mRNA
274 expression in the acute HFRS patients, similar with the finding from severe
275 COVID-19 cohorts (Haslund-Gourley et al., 2024). The neuraminidase 1 (NEU1)
276 gene is strikingly upregulated and may potentially explain the decreased sialylation on
277 the secreted HTNV-specific IgG antibodies during convalescence. Overall, the
278 glycosylation of immunoglobulin G is regulated by a large network of B-cell
279 glycogenes during HTNV infection.

280 Despite establishing a well-characterized patient cohort and performing systematic
281 IgG glycosylation profiling based on HTNV NP antibody status, this study has several
282 noteworthy limitations. Most notably, while preliminary comparisons suggested

283 similar patterns between virus-specific and total IgG N-glycome, our total plasma IgG
284 analysis may have introduced confounding factors in the observed associations. This
285 methodological constraint could potentially affect the interpretation of certain
286 disease-specific glycosylation signatures.

287 Our findings demonstrate that the IgG-Fc glycosylation plays a pivotal role in
288 HTNV infection and rapid recovery. Fucosylated oligosaccharides and the absence of
289 bisecting GlcNAc are associated with favorable clinical outcomes. Importantly,
290 specific B cell subsets, particularly ASMs and PBs, upregulated the secretion of
291 galactosylated and sialylated antibodies, respectively. These findings would deepen
292 our understanding of antibody glycosylation in antivirus immunity and provide a
293 foundation for future studies aimed at optimizing glycoengineered therapeutic
294 antibodies.

295 **Materials and Methods**

296 **Study participants**

297 Clinical specimens were collected from HFRS patients who were hospitalized in
298 Baoji Central Hospital between October 2019 and January 2022. Patients were
299 categorized into four clinical subtypes (mild, moderate, severe, and critical) based on
300 the diagnostic criteria for HFRS issued by the Ministry of Health (Ma et al., 2015).
301 This study was approved by the ethics committee of the Shandong First Medical
302 University & Shandong Academy of Medical Sciences (R201937). Written informed
303 consent was obtained from each participant or their guardians.

304 The clinical course of HFRS is grouped into acute (febrile, hypotensive, and
305 oliguric stages) and convalescent (diuretic and convalescent stages) phases. The acute
306 phase was defined as within 12 days of illness onset, and the convalescent phase was
307 defined as a period of illness lasting 13 days or longer (Tang et al., 2019; Zhang et al.,

308 2022). The earliest sample was selected if there were multiple blood samples
309 available in the acute phase and the last available sample before discharge was
310 selected if there were multiple blood samples in the convalescent phase.

311 **Single-Cell RNA Sequencing and public database**

312 Flow cytometry antibody staining was conducted as previously described
313 (Chakraborty et al., 2022). Dead cell and red blood cell were removed using the BD
314 FACSAria™ III cell sorter, and peripheral blood mononuclear cells (PBMCs) were
315 collected for single-cell sequencing. The library construction was conducted as
316 previously described (Jin et al., 2024).

317 We obtained single-cell transcriptome sequencing data from the Gene Expression
318 Omnibus (GEO) database (GSE161354), containing six HFRS patients and two
319 healthy volunteers, as well as healthy control samples from the Genome Sequence
320 Archive (GSA) database (HRA000203), matched with patient demographic
321 information.

322 **Single-Cell Data Analysis**

323 The FastQC software was used to evaluate the data obtained to ensure the quality of
324 the raw sequencing data. The raw data were mapped to the human reference genome
325 (GRCh38, https://cf.10xgenomics.com/supp/cell-exp/refdata-gex-GRCh38-2020-A.tar.
326 gz) using Cell Ranger. The Seurat R package (Version 4.4.0) was utilized for the
327 merging and clustering of single-cell data. The Harmony R package and the anchor
328 module of Seurat were used to remove batch effects between samples and groups for
329 cell clustering. t-distributed Stochastic Neighbor Embedding (t-SNE) and Uniform
330 Manifold Approximation and Projection (UMAP) were employed for dimensionality
331 reduction and visualization of individual cells.

332 **Cell Type Annotation**

333 UMAP and t-SNE were used to reduce the dimension of all cells and to cluster
334 them in a two-dimensional space based on shared features. The Single R (Version
335 2.2.0) package was used to infer independently the cell origin of each single cell
336 based on a reference transcriptome dataset of pure cell types, for unbiased cell type
337 identification from single-cell RNA sequencing data. Subsequently, specific
338 highly-expressed genes were combined with those derived from review of the
339 literature for manual annotation to ultimately determine cell types. Classic biomarkers
340 for specific cell types were used to identify cells in different clusters.

341 **Differential Gene Identification and Functional Analysis**

342 The *FindMarkers()* function in the Seurat package was used to identify DEGs
343 between different cell groups, with criteria of |log2FC| > 0.25 and p-value<0.05,
344 pct.1>0.25. The ClusterProfiler R package was utilized for GO, KEGG, and GSEA
345 enrichment analyses, and the ggplot2 and enrichplot R packages were used for
346 visualization.

347 **Measurement of HTNV specific antibodies**

348 Levels of serum IgM and IgG antibodies to HTNV NP were assessed through the
349 enzyme-linked immunosorbent assay (ELISA) kit (Wantai BioPharm, Beijing, China)
350 in accordance with the manufacturer's instructions.

351 **Analysis of IgG glycans**

352 The process of isolating, labelling, purifying, and analyzing plasma IgG was
353 performed using previously established methods (Hou et al., 2019; Pengcheng Liu,
354 2023). Briefly, the diluted plasma samples were transferred onto a 96-well protein G
355 monolithic plate (BIA Separations, Slovenia) for the isolation of IgG. The isolated
356 IgG was eluted with 1 mL of 0.1 M formic acid and was immediately neutralized with
357 170 μL of 1M ammonium bicarbonate.

358 The released N-glycans were labelled with 2-aminobenzamide (2-AB) and were
359 then purified from a mixture of 100% acetonitrile and ultrapure water in a 1:1 ratio
360 (v/v). This was then analyzed by hydrophilic interaction liquid chromatography using
361 ultra-performance liquid chromatography (HILIC-UPLC; Walters Corporation,
362 Milford, MA) (Hou et al., 2019). As previously reported, the chromatograms were
363 separated into 24 IgG glycan peaks (GPs) (Menni et al., 2018).

364 Our study incorporated both biological and technical replicates to ensure a robust
365 glycomic profiling analysis. Specifically, we analyzed paired
366 acute/convalescent-phase samples from 65 confirmed HFRS patients to assess
367 inter-individual biological variability, while technical reproducibility was validated
368 through comparison with standard chromatographic peak plots (Vučković et al., 2016).
369 This dual-replicate strategy enabled a comprehensive evaluation of both biological
370 heterogeneity and assay precision, and the coefficient of variation for samples were
371 below 16%.

372 **Virus-specific B-cell detection**

373 Virus-specific B-cell against HTNV were performed as previously described
374 (Liechti & Roederer, 2019; Song et al., 2018).

375 **Statistical analysis**

376 Categorical variables were compared using chi-square tests. Normality of numeric
377 variables was assessed with the Kolmogorov-Smirnov test; non-normally distributed
378 continuous variables were analyzed using non-parametric tests. The Benjamini -
379 Hochberg (BH) method was used to adjust the raw p-values from DEG analysis,
380 controlling the false discovery rate (FDR). Statistical analyses were performed with R
381 software version 4.1.1 (R Core Team, New Zealand) and GraphPad Prism 8
382 (GraphPad Software, San Diego, CA), with a significance level of $\alpha = 0.05$

383 (two-tailed).

384 **Author contributions**

385 Haifeng Hou and Weifeng Shi designed and supervised this study. Chuansong
386 Quan, Lu Wang, Jiming Gao, Yaoni Li, Houqiang Li, Hongzhi Liu, Qian Li, and
387 Liqiong Zhao collected the samples and performed experiments. Chuansong Quan, Lu
388 Wang, Jiming Gao, Xiaoyu Xu, Zixuan Gao, Wenxu Ruan, and Weijia Xing analyzed
389 the data and performed the statistical analyses. Lu Wang, Chuansong Quan, Jiming
390 Gao, and Xiaoyu Xu wrote the manuscript. Haifeng Hou, Weifeng Shi, Weijia Xing,
391 and Michael J. Carr reviewed and edited the manuscript. All authors had full access to
392 all of the data in the study and accept responsibility for the decision to submit for
393 publication.

394 **Funding**

Funder	Grant reference number	Author
the Natural Science Foundation of Shandong Province	Grant numbers ZR2020QH133	Chuansong Quan
the Natural Science Foundation of Shandong Province	Grant numbers ZR2022MH082	Haifeng Hou
the Natural Science Foundation of Shandong Province	Grant numbers ZR2024MH235	Weijia Xing
the Natural Science Foundation of Shandong Province	Grant numbers ZR201911090028	Yaoni Li
Shaanxi Provincial Natural Science Basic Research Program of Shaanxi Province	Grant number 2023-JC-YB-741	Yaoni Li

395 **Data availability**

396 The data underlying this article will be shared upon request to the corresponding
397 author.

398 The following dataset was generated:

Author(s)	Year	Dataset title	Dataset URL	Database and Identifier
Chuansong Quan	2025	Glycosylated IgG antibodies accelerated the recovery of haemorrhagic fever with renal syndrome patients	https://www.ncbi.nlm.nih.gov/sra/PRJNA1238574	Sequence Read Archive, PRINA1238574

Zhang H, Wang Y (2022) **Increased CD4^{+}CD8^{+} double positive T cells during Hantaan virus infection** ID GSE161354. In the public domain at GEO http://www.ncbi.nlm.nih.gov/geo/. https://www.ncbi.nlm.nih.gov/geo/query/acc.cgi?acc=GSE161354.

Zheng Y, Liu X (2020) **A human circulating immune cell landscape in aging and COVID-19** ID HRA000203. In the public domain at GSA https://ngdc.cncb.ac.cn/search/.

https://ngdc.cncb.ac.cn/gsa-human/browse/HRA000203.

Disclosure statement

No potential conflict of interest was reported by the author(s).

References

Zheng, Z., Wang, P., Wang, Z., Zhang, D., Wang, X., Zuo, S., & Li, X. (2019). The characteristics of current natural foci of hemorrhagic fever with renal syndrome in Shandong Province, China, 2012-2015. PLoS Negl Trop Dis, 13(5), e0007148. doi:10.1371/journal.pntd.0007148

Li, R., Sun, J., Chen, Y., Fan, X., Wang, X., Zhang, X., . . . Liu, Z. (2023). Clinical and laboratory features and factors predicting disease severity in pediatric patients with hemorrhagic fever with renal syndrome caused by Hantaan virus. J Med Virol, 95(1), e28339. doi:10.1002/jmv.28339

Pizarro, E., Navarrete, M., Mendez, C., Zaror, L., Mansilla, C., Tapia, M., . . . Rodríguez, E. M. (2019). Immunocytochemical and ultrastructural evidence supporting that Andes Hantavirus (ANDV) is transmitted person-to-person through the respiratory and/or salivary pathways. Front Microbiol, 10, 2992. doi:10.3389/fmicb.2019.02992

Tariq, M., & Kim, D. M. (2022). Hemorrhagic fever with renal syndrome: literature review, epidemiology, clinical picture and pathogenesis. Infect Chemother, 54(1), 1–19. doi:10.3947/ic.2021.0148

Engdahl, T. B., & Crowe, J. E., Jr. (2020). Humoral immunity to Hantavirus infection. mSphere, 5(4). doi:10.1128/mSphere.00482-20

Li, Y., Quan, C., Xing, W., Wang, P., Gao, J., Zhang, Z., . . . Shi, W. (2020). Rapid humoral immune responses are required for recovery from haemorrhagic fever with renal syndrome patients. Emerg Microbes Infect, 9(1), 2303 – 2314. doi:10.1080/22221751.2020.1830717

Ash, M. K., Bhimalli, P. P., Cho, B. K., Mattamana, B. B., Gambut, S., Tarhoni, I., . . . Schneider, J. R. (2022). Bulk IgG glycosylation predicts COVID-19 severity

434 and vaccine antibody response. Cell Rep, 41(11), 111799.
435 doi:10.1016/j.celrep.2022.111799
436 Haslund-Gourley, B. S., Woloszczuk, K., Hou, J., Connors, J., Cusimano, G., Bell,
437 M., . . . Comunale, M. A. (2024). IgM N-glycosylation correlates with COVID-19
438 severity and rate of complement deposition. Nat Commun, 15(1), 404.
439 doi:10.1038/s41467-023-44211-0
440 Hou, H., Yang, H., Liu, P., Huang, C., Wang, M., Li, Y., . . . Wang, W. (2021).
441 Profile of immunoglobulin G N-glycome in COVID-19 patients: a case-control study.
442 Front Immunol, 12, 748566. doi:10.3389/fimmu.2021.748566
443 Wang, T. T., Sewatanon, J., Memoli, M. J., Wrammert, J., Bournazos, S., Bhaumik,
444 S. K., . . . Ravetch, J. V. (2017). IgG antibodies to dengue enhanced for FcγRIIIA
445 binding determine disease severity. Science, 355(6323), 395 – 398.
446 doi:10.1126/science.aai8128
447 Onwuchekwa, C., Moreo, L. M., Menon, S., Machado, B., Curcio, D., Kalina,
448 W., . . . Begier, E. (2023). Underascertainment of respiratory syncytial virus infection
449 in adults due to diagnostic testing limitations: a systematic literature review and
450 meta-analysis. J Infect Dis, 228(2), 173–184. doi:10.1093/infdis/jiad012
451 Larsen, M. D., de Graaf, E. L., Sonneveld, M. E., Plomp, H. R., Nouta, J., Hoepel,
452 W., . . . Vidarsson, G. (2021). Afucosylated IgG characterizes enveloped viral
453 responses and correlates with COVID-19 severity. Science, 371(6532).
454 doi:10.1126/science.abc8378
455 Lu, L. L., Suscovich, T. J., Fortune, S. M., & Alter, G. (2018). Beyond binding:
456 antibody effector functions in infectious diseases. Nat Rev Immunol, 18(1), 46−61.
457 doi:10.1038/nri.2017.106
458 Wieczorek, M., Braicu, E. I., Oliveira-Ferrer, L., Sehouli, J., & Blanchard, V.

459 (2020). Immunoglobulin G subclass-specific glycosylation changes in primary
460 epithelial ovarian cancer. Front Immunol, 11, 654. doi:10.3389/fimmu.2020.00654
461 Giron, L. B., Colomb, F., Papasavvas, E., Azzoni, L., Yin, X., Fair, M., . . .
462 Abdel-Mohsen, M. (2020). Interferon-α alters host glycosylation machinery during
463 treated HIV infection. EBioMedicine, 59, 102945. doi:10.1016/j.ebiom.2020.102945
464 Irvine, E. B., & Alter, G. (2020). Understanding the role of antibody glycosylation
465 through the lens of severe viral and bacterial diseases. Glycobiology, 30(4), 241–253.
466 doi:10.1093/glycob/cwaa018
467 Ackerman, M. E., Das, J., Pittala, S., Broge, T., Linde, C., Suscovich, T. J., . . .
468 Alter, G. (2018). Route of immunization defines multiple mechanisms of
469 vaccine-mediated protection against SIV. Nat Med, 24(10), 1590 – 1598.
470 doi:10.1038/s41591-018-0161-0
471 Jennewein, M. F., & Alter, G. (2017). The immunoregulatory roles of antibody
472 glycosylation. Trends Immunol, 38(5), 358–372. doi:10.1016/j.it.2017.02.004
473 Liu, D., Chu, X., Wang, H., Dong, J., Ge, S. Q., Zhao, Z. Y., . . . Wang, W. (2018).
474 The changes of immunoglobulin G N-glycosylation in blood lipids and dyslipidaemia.
475 J Transl Med, 16(1), 235. doi:10.1186/s12967-018-1616-2
476 Houde, D., Peng, Y., Berkowitz, S. A., & Engen, J. R. (2010). Post-translational
477 modifications differentially affect IgG1 conformation and receptor binding. Mol Cell
478 Proteomics, 9(8), 1716–1728. doi:10.1074/mcp.M900540-MCP200
479 Hwang, H. J., Kang, D., Shin, J., Jung, J., Ko, S., Jung, K. H., . . . Lee, J. S. (2025).
480 Therapy-induced senescent cancer cells contribute to cancer progression by
481 promoting ribophorin 1-dependent PD-L1 upregulation. Nat Commun, 16(1), 353.
482 doi:10.1038/s41467-024-54132-1
483 Wang, T. T., & Ravetch, J. V. (2019). Functional diversification of IgGs through Fc

484 glycosylation. J Clin Invest, 129(9), 3492–3498. doi:10.1172/jci130029

485 Yang, Z., Wang, S., Halim, A., Schulz, M. A., Frodin, M., Rahman, S. H., . . .
486 Clausen, H. (2015). Engineered CHO cells for production of diverse, homogeneous
487 glycoproteins. Nat Biotechnol, 33(8), 842–844. doi:10.1038/nbt.3280

488 Ma, Y., Yuan, B., Zhuang, R., Zhang, Y., Liu, B., Zhang, C., . . . Jin, B. (2015).
489 Hantaan virus infection induces both Th1 and ThGranzyme B+ cell immune responses
490 that associated with viral control and clinical outcome in humans. PLoS Pathog, 11(4),
491 e1004788. doi:10.1371/journal.ppat.1004788

492 Tang, K., Zhang, C., Zhang, Y., Zhang, Y., Du, H., Jin, B., & Ma, Y. (2019).
493 Elevated plasma interleukin 34 levels correlate with disease severity-reflecting
494 parameters of patients with haemorrhagic fever with renal syndrome. Infect Dis
495 (Lond), 51(11-12), 847–853. doi:10.1080/23744235.2019.1672887

496 Zhang, H., Wang, Y., Ma, Y., Tang, K., Zhang, C., Wang, M., . . . Zhang, Y. (2022).
497 Increased CD4(+)CD8(+) double positive T cells during Hantaan virus infection.
498 Viruses, 14(10). doi:10.3390/v14102243

499 Chakraborty, S., Gonzalez, J. C., Sievers, B. L., Mallajosyula, V., Chakraborty, S.,
500 Dubey, M., . . . Wang, T. T. (2022). Early non-neutralizing, afucosylated antibody
501 responses are associated with COVID-19 severity. Sci Transl Med, 14(635),
502 eabm7853. doi:10.1126/scitranslmed.abm7853

503 Jin, C., Chen, Y., Wang, Y., Li, J., Liang, J., Zheng, S., . . . Yang, H. (2024).
504 Single-cell RNA sequencing reveals special basal cells and fibroblasts in idiopathic
505 pulmonary fibrosis. Sci Rep, 14(1), 15778. doi:10.1038/s41598-024-66947-5

506 Hou, H., Xu, X., Sun, F., Zhang, X., Dong, H., Wang, L., . . . Wang, Y. (2019).
507 Hyperuricemia is associated with immunoglobulin G N-glycosylation: a
508 community-based study of glycan biomarkers. Omics, 23(12), 660 – 667.

509 doi:10.1089/omi.2019.0004

510 Pengcheng Liu, X. W., Aishe Dun, Yutong Li, Houqiang Li, Lu Wang, Yichun
511 Zhang, Cancan Li, Jinxia Zhang, Xiaoyu Zhang, Lixing Ma f, Haifeng Hou. (2023).
512 High-throughput profiling of serological immunoglobulin G N-glycome as a
513 noninvasive biomarker of gastrointestinal cancers. Engineering, 26(7), 44 – 53.
514 doi:10.1016/j.eng.2023.02.008

515 Menni, C., Gudelj, I., Macdonald-Dunlop, E., Mangino, M., Zierer, J., Bešić, E., . . .
516 Valdes, A. M. (2018). Glycosylation profile of immunoglobulin G is cross-sectionally
517 associated with cardiovascular disease risk score and subclinical atherosclerosis in
518 two independent cohorts. Circ Res, 122(11), 1555 – 1564.
519 doi:10.1161/circresaha.117.312174

520 Vučković, F., Theodoratou, E., Thaçi, K., Timofeeva, M., Vojta, A., Štambuk, J., . . .
521 Lauc, G. (2016). IgG glycome in colorectal cancer. Clin Cancer Res, 22(12), 3078–
522 3086. doi:10.1158/1078-0432.Ccr-15-1867

523 Liechti, T., & Roederer, M. (2019). OMIP-051 - 28-color flow cytometry panel to
524 characterize B cells and myeloid cells. Cytometry A, 95(2), 150 – 155.
525 doi:10.1002/cyto.a.23689

526 Song, P., Zheng, N., Liu, Y., Tian, C., Wu, X., Ma, X., . . . Wu, Z. (2018). Deficient
527 humoral responses and disrupted B-cell immunity are associated with fatal SFTSV
528 infection. Nat Commun, 9(1), 3328. doi:10.1038/s41467-018-05746-9

529 **Figure legends**

530 **Figure 1. Flow chart of HFRS patient recruitment in Baoji Central Hospital in**
531 **Shaanxi province from November 2019 to January 2022.**

532 **Figure 2. Immunophenotypic remodeling in the B-cell subsets during acute**
533 **HFRS.**

534 (A) t-distributed stochastic neighbor embedding (t-SNE) plot showing antibody
535 secreting memory B cells (ASM), double negative (DN) B cells, intermediate memory
536 cells (IM), marginal zone-like cells (MZB), naive B cells, plasmablasts (PB),
537 quiescent resting memory cells (RM), and exhausted tissue-like memory B cells
538 (TLM) of PBMCs identified using an integrated and classification analysis. (B) t-SNE
539 projection of canonical markers, including CD19, CD27, CD38, IgD, and IgM. (C)
540 Proportions of the eight B cell subsets, colored by the healthy group (green) and
541 HTNV groups (red). Boxplot features: minimum box, 25th percentile; center, median;
542 maximum box, 75th percentile. (D) Frequency of the eight B cell subsets in between
543 the healthy group (n = 8) and HTNV groups (n = 15). (E) FACS gating strategy for
544 the measurement of the B-cell subsets: activated memory B cells ($CD21^-$ $CD27^+$, AM),
545 RM B cells ($CD21^+$ $CD27^+$), IM B cells ($CD21^+$ $CD27^-$), TLM B cells ($CD21^-$ $CD27^-$),
546 naive B cells ($CD27^-$ IgD^+), MZB B cells ($CD27^+$ IgD^+), ASM B cells ($CD27^+$ IgD^-),
547 DN B cells ($CD27^-$ IgD^-), PB ($CD38^+$ $CD27^+$), and class-switched memory B cells
548 ($CD38^-$ $CD27^+$, CSM), respectively. (F) The proportion of ASM, CSM, naive B, and
549 PB cells in $CD19^+$ B cells in the acute and convalescent HFRS patients. Data are
550 presented as mean ± SEM in panels C and F. *$p<0.05$ (Student's t-test).

551 **Figure 3. Glycosylation modification of antibodies associated with HTNV**
552 **infection.** (A) Changes of different glycosylation types in both HTNV NP-specific
553 IgG negative and positive plasma from 24 HFRS patients. (B) Differential IgG

554 glycosylation patterns across antibody titer levels quantified by ELISA. (C)
555 Comparison of different glycosylation levels before and after the fourfold increase in
556 the IgG antibody titers. *p<0.05, **p<0.01, ***p<0.001. For paired samples,
557 Wilcoxon Signed Rank Test was used to assess the difference.

558 **Figure 4. Glycosylation modifications of antibodies primarily deprived from**
559 **antibody-secreting and plasmablast subpopulations.**

560 (A) The correlation between the proportion of PB cells and the sialylation level. (B)
561 The correlation between the proportion of ASM cells and the sialylation level. (C) The
562 correlation between the proportion of ASM cells and the galactosylation level. (D)
563 Dot plot shows the expression levels of glycosylation-related genes in the eight B cell
564 groups. The pink color represents mannose related genes, the green color represents
565 N-glycosylation-related genes, the orange color represents galactosylation-related
566 genes, the purple represents sialylation-related genes, and the red color represents
567 fucosylation related genes. (E) Enriched pathways in the plasmablast and ASM
568 subsets by GO enrichment analysis of the DEGs. (F) The GSEA map presents the
569 enrichment score of GRGs in N-Glycan biosynthesis.

570 **Supplementary materials**

571 **Supplementary file 1. The proportion of different B cell subpopulations between**
572 **healthy and acute HFRS groups.**

573 **Supplementary file 2. Difference in main IgG glycome features of HFRS patients**
574 **between age groups.**

575 **Supplementary file 3. Difference in main IgG glycome features of HFRS patients**
576 **between sex groups.**

577 **Supplementary file 4. Relative abundance (%) of the main IgG-Fc glycome**
578 **features in HFRS patients.**

579 **Supplementary file 5. Results of multiple linear regression analysis**
580 **for fucosylation.**

581 APTT, activated partial thromboplastin time; MCHC, mean corpuscular hemoglobin
582 concentration; NEUT, neutrophil; PLT, platelet; WBC, white blood cell; CRE,
583 creatinine; Cys-C, cystatin C.

584 **Supplementary file 6. Results of multiple linear regression analysis for bisecting**
585 **GlcNAc.**

586 APTT, activated partial thromboplastin time; MCHC, mean corpuscular hemoglobin
587 concentration; NEUT, neutrophil; PLT, platelet; WBC, white blood cell; CRE,
588 creatinine; Cys-C, cystatin C.

589 **Supplementary file 7. Results of multiple linear regression analysis**
590 **for galactosylation.**

591 APTT, activated partial thromboplastin time; MCHC, mean corpuscular hemoglobin
592 concentration; NEUT, neutrophil; PLT, platelet; WBC, white blood cell; CRE,
593 creatinine; Cys-C, cystatin C.

594 **Supplementary file 8. Results of multiple linear regression analysis**
595 **for sialylation.**
596 APTT, activated partial thromboplastin time; MCHC, mean corpuscular hemoglobin
597 concentration; NEUT, neutrophil; PLT, platelet; WBC, white blood cell; CRE,
598 creatinine; Cys-C, cystatin C.
599 **Supplementary file 9. Differentially expressed genes among different B cell**
600 **subgroups in healthy and acute HFRS groups.**
601 **Supplementary file 10. Differential expression genes in the ASM, PB and RM B**
602 **cell subpopulations.**
603 **Supplementary file 11. Differential expression genes in the DN, IM and naive B**
604 **cell subpopulations.**
605
606 **Figure 2—figure supplement 1. Single-cell transcriptomes of PBMCs from**
607 **patients with HFRS.**
608 (A) Uniform manifold approximation and projection (UMAP) presentation of the
609 major peripheral immune cell types in the PBMCs from 15 HFRS patients and 8
610 healthy controls. (B) Dot plot shows the expression levels of canonical marker-related
611 genes in the different subpopulations. (C) UMAP presentation of the major peripheral
612 immune cell types among HFRS and healthy control groups. (D) Proportions of the
613 eight cell subsets, colored by the healthy group (green) and HTNV groups (red).
614 Boxplot features: minimum box, 25th percentile; center, median; maximum box, 75th
615 percentile. (E) Frequency of the eight cell subsets in between the healthy group (n = 8)
616 and the HTNV group (n = 15). (F) The UMAP plot shows the differentiation
617 trajectories of different cell types calculated by pseudotime analysis.
618 **Figure 2—figure supplement 2. Dynamic analysis of the B-cell subsets in HFRS**

619 **patients.**

620 (A) Expression of MZB in $CD19^+$ B cells. (B) Expression of DN in $CD19^+$ B cells.
621 (C) Expression of TLM in $CD19^+$ B cells. (D) Expression of AM in $CD19^+$ B cells. (E)
622 Expression of RM in $CD19^+$ B cells. (F) Expression of IM in $CD19^+$ B cells.

623 **Figure 4—figure supplement 1. The differentially expressed genes and their**
624 **functional changes in the B cell subsets post HTNV infection.**

625 (A) The volcano plot shows the differentially expressed genes of different B cell
626 subsets in acute HFRS patients. The red font represents the upregulation of the B cell
627 subpopulations, and the blue font represents the downregulation of the B cell
628 subpopulations. (B and C) The volcano plot displays the differentially expressed
629 genes in upregulation B cell subpopulations including antibody secreting memory B
630 cells, plasmablasts, and quiescent resting memory B cells (B), and downregulation B
631 cell subpopulations including naive B cells, double negative B cells, and intermediate
632 memory B cells (C).

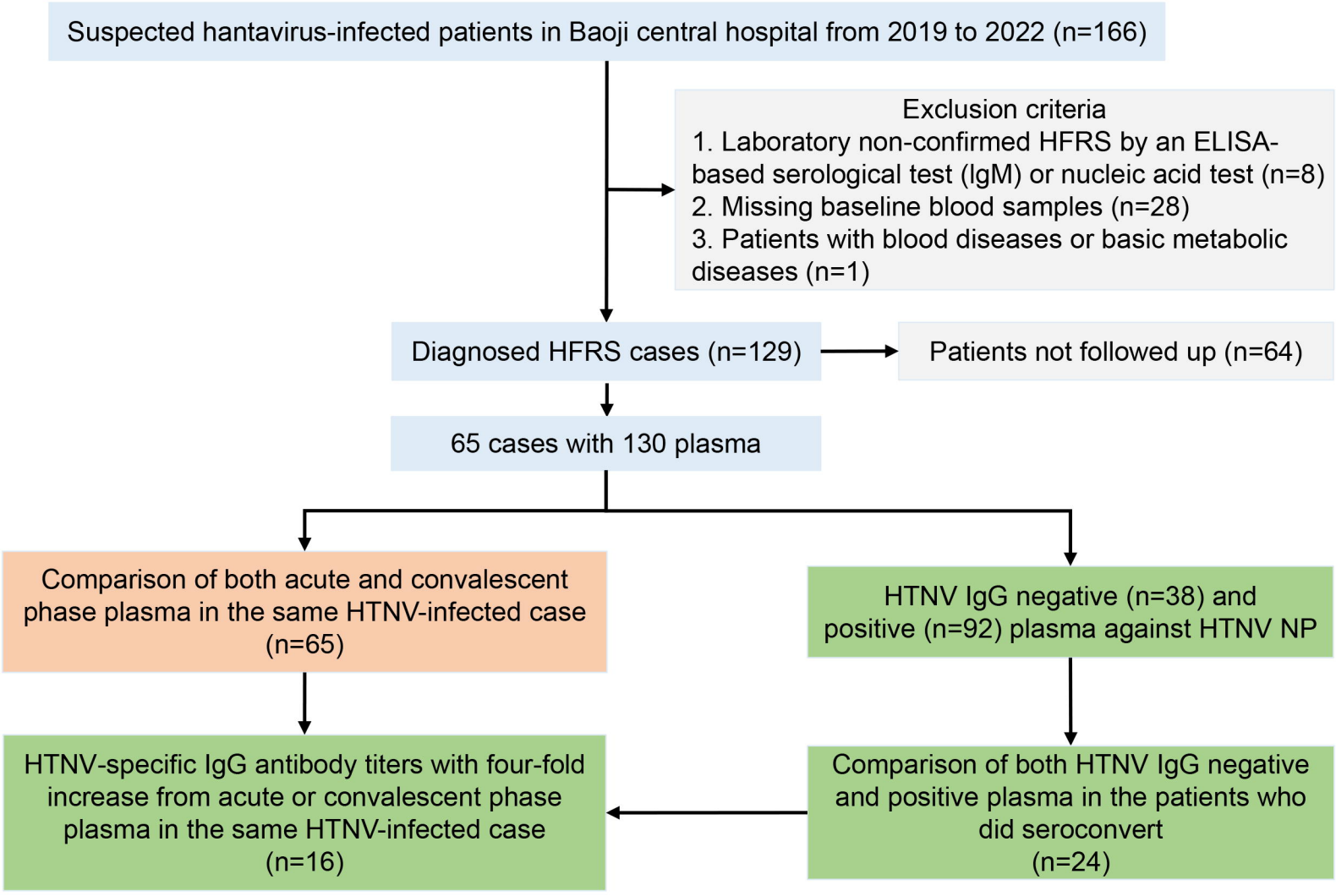
Suspected hantavirus-infected patients in Baoji central hospital from 2019 to 2022 (n=166)
Exclusion criteria
1. Laboratory non-confirmed HFRS by an ELISA-based serological test (IgM) or nucleic acid test (n=8)
2. Missing baseline blood samples (n=28)
3. Patients with blood diseases or basic metabolic diseases (n=1)
Diagnosed HFRS cases (n=129)
Patients not followed up (n=64)
65 cases with 130 plasma
Comparison of both acute and convalescent phase plasma in the same HTNV-infected case (n=65)
HTNV IgG negative (n=38) and positive (n=92) plasma against HTNV NP
HTNV-specific IgG antibody titers with four-fold increase from acute or convalescent phase plasma in the same HTNV-infected case (n=16)
Comparison of both HTNV IgG negative and positive plasma in the patients who did seroconvert (n=24)

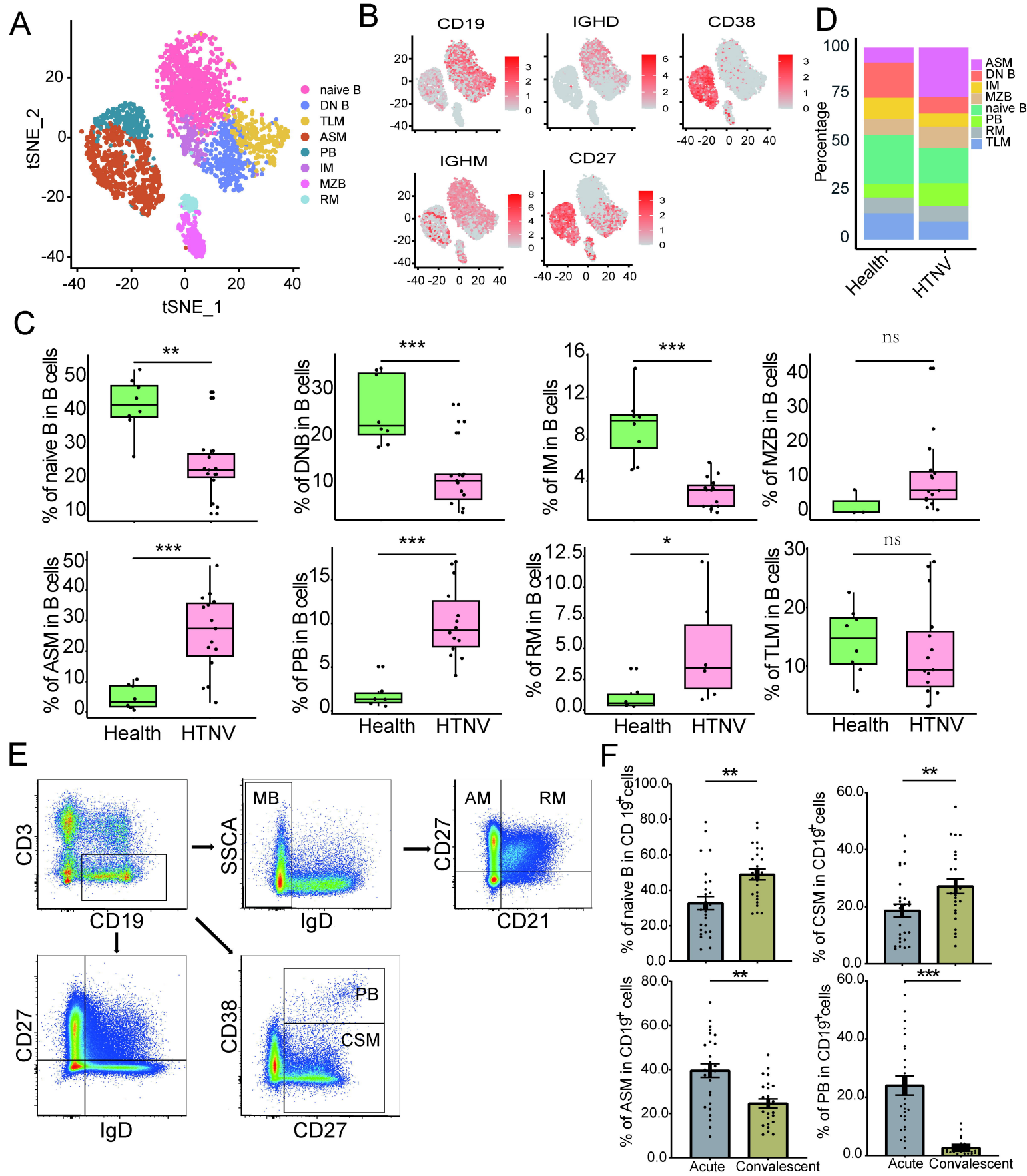
A
tSNE_2
tSNE_1
naive B
DN B
TLM
ASM
PB
IM
MZB
RM
B
CD19
IGHD
CD38
IGHM
CD27
D
Percentage
Health
HTNV
C
% of naive B in B cells
% of DNB in B cells
% of IM in B cells
% of MZB in B cells
% of ASM in B cells
% of PB in B cells
% of RM in B cells
% of TLM in B cells
ns
E
CD3
CD19
SSCA
MB
IgD
CD27
AM
RM
CD21
PB
CSM
CD38
F
% of naive B in CD 19+cells
% of CSM in CD19+cells
% of ASM in CD19+ cells
% of PB in CD19+cells
Acute
Convalescent

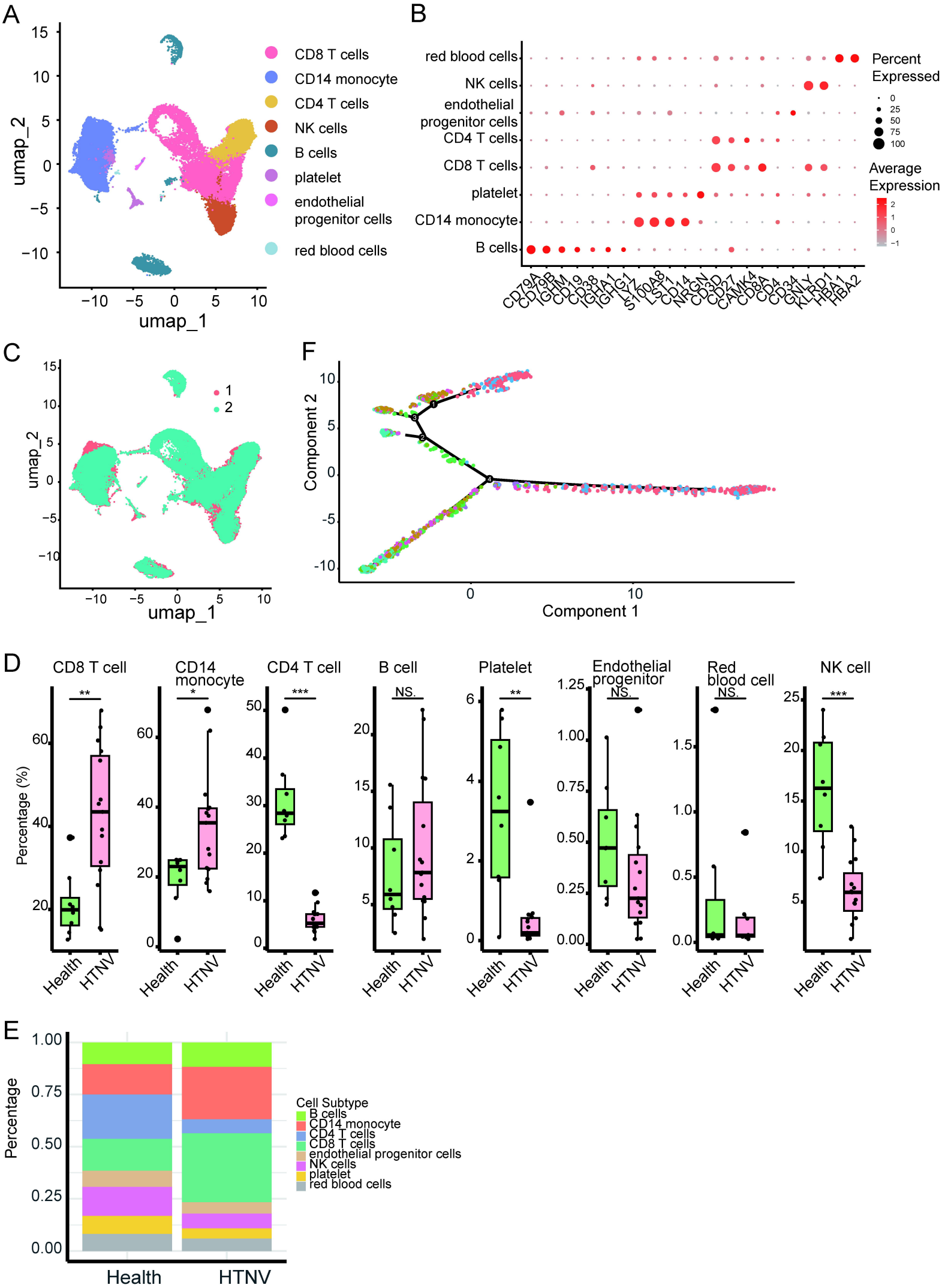
A
umap_2
umap_1
CD8 T cells
CD14 monocyte
CD4 T cells
NK cells
B cells
platelet
endothelial progenitor cells
red blood cells
B
Percent Expressed
Average Expression
CD79A
CD79B
IGHM
CD19
CD38
IGHA1
IGHG1
LYZ
S100A8
LST1
CD14
NRGN
CD3D
CD27
CAMK4
CD8A
CD4
CD34
GNLY
KLRD1
HBA1
HBA2
C
F
Component 1
Component 2
D
CD8 T cell
CD14 monocyte
CD4 T cell
B cell
Platelet
Endothelial progenitor
Red blood cell
NK cell
Percentage (%)
Health
HTNV
E
Percentage
Cell Subtype
B cells
CD14 monocyte
CD4 T cells
CD8 T cells
endothelial progenitor cells
NK cells
platelet
red blood cells

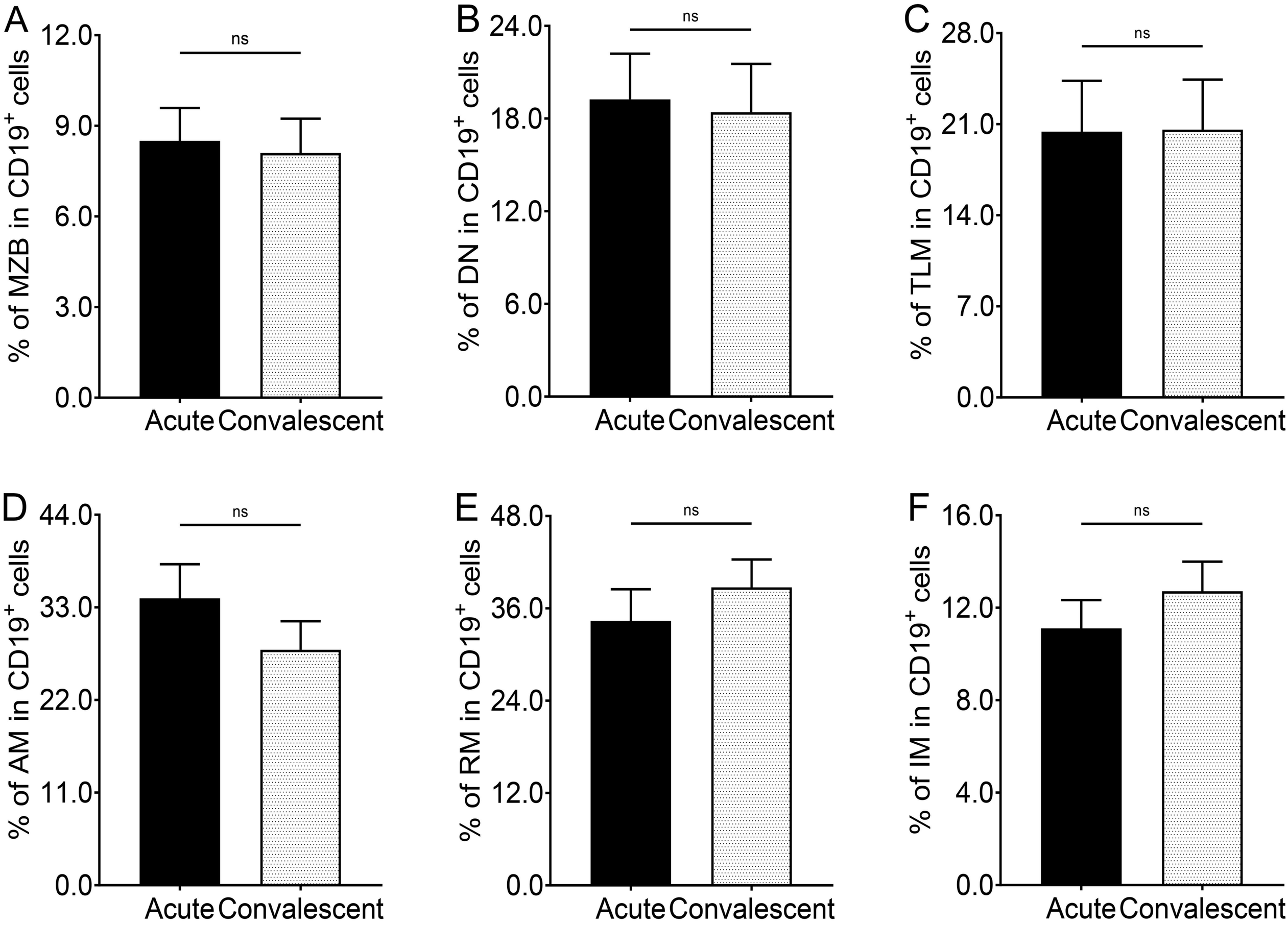
A
% of MZB in CD19+ cells
12.0
9.0
6.0
3.0
0.0
ns
Acute
Convalescent
B
% of DN in CD19+ cells
24.0
18.0
12.0
6.0
0.0
ns
Acute
Convalescent
C
% of TLM in CD19+ cells
28.0
21.0
14.0
7.0
0.0
ns
Acute
Convalescent
D
% of AM in CD19+ cells
44.0
33.0
22.0
11.0
0.0
ns
Acute
Convalescent
E
% of RM in CD19+ cells
48.0
36.0
24.0
12.0
0.0
ns
Acute
Convalescent
F
% of IM in CD19+ cells
16.0
12.0
8.0
4.0
0.0
ns
Acute
Convalescent

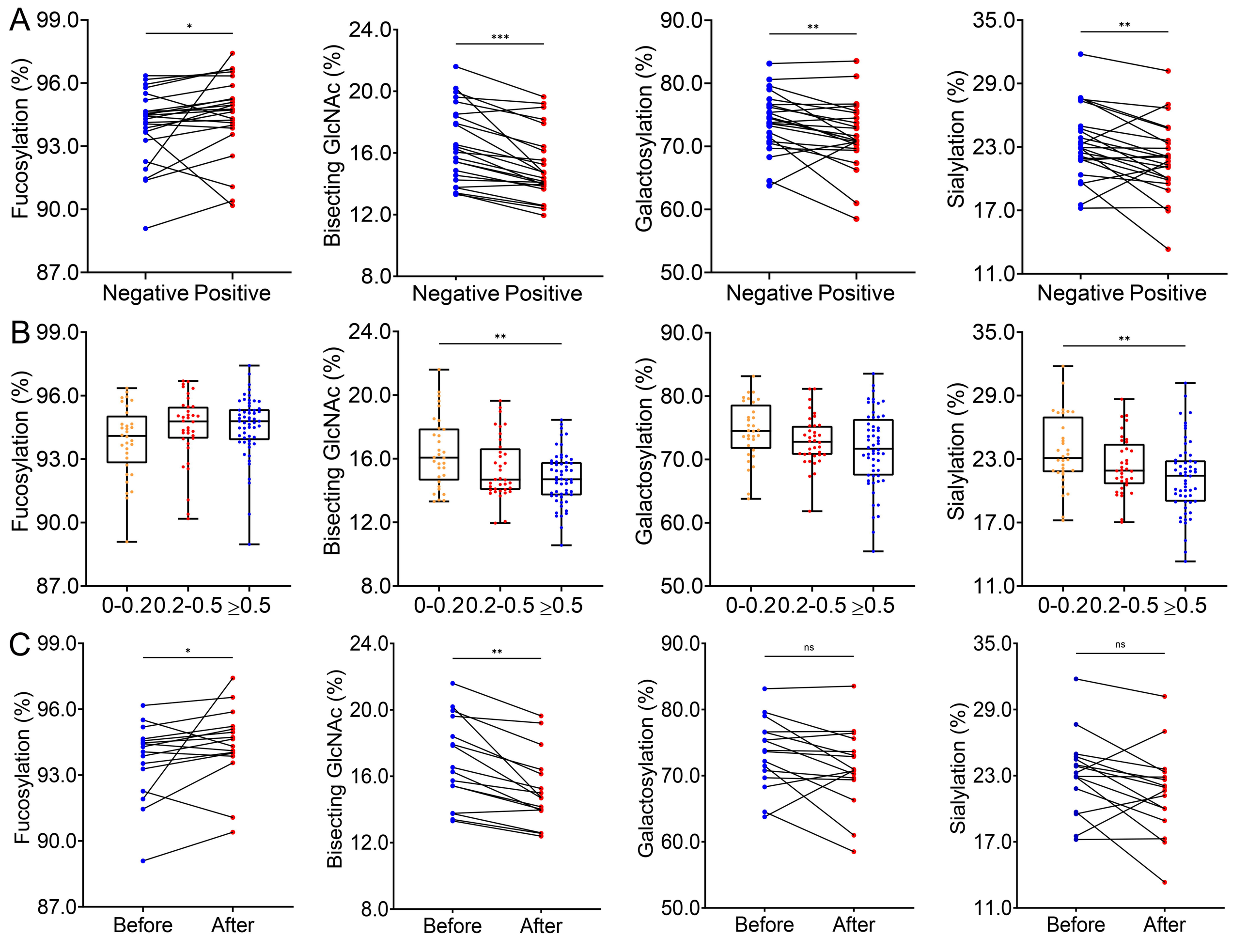
A
Fucosylation (%)
99.0
96.0
93.0
90.0
87.0
*
Negative Positive
Bisecting GlcNAc (%)
24.0
20.0
16.0
12.0
8.0
***
Negative Positive
Galactosylation (%)
90.0
80.0
70.0
60.0
50.0
**
Negative Positive
Sialylation (%)
35.0
29.0
23.0
17.0
11.0
**
Negative Positive
B
Fucosylation (%)
99.0
96.0
93.0
90.0
87.0
0-0.2 0.2-0.5 ≥0.5
Bisecting GlcNAc (%)
24.0
20.0
16.0
12.0
8.0
**
0-0.2 0.2-0.5 ≥0.5
Galactosylation (%)
90.0
80.0
70.0
60.0
50.0
0-0.2 0.2-0.5 ≥0.5
Sialylation (%)
35.0
29.0
23.0
17.0
11.0
**
0-0.2 0.2-0.5 ≥0.5
C
Fucosylation (%)
99.0
96.0
93.0
90.0
87.0
*
Before After
Bisecting GlcNAc (%)
24.0
20.0
16.0
12.0
8.0
**
Before After
Galactosylation (%)
90.0
80.0
70.0
60.0
50.0
ns
Before After
Sialylation (%)
35.0
29.0
23.0
17.0
11.0
ns
Before After

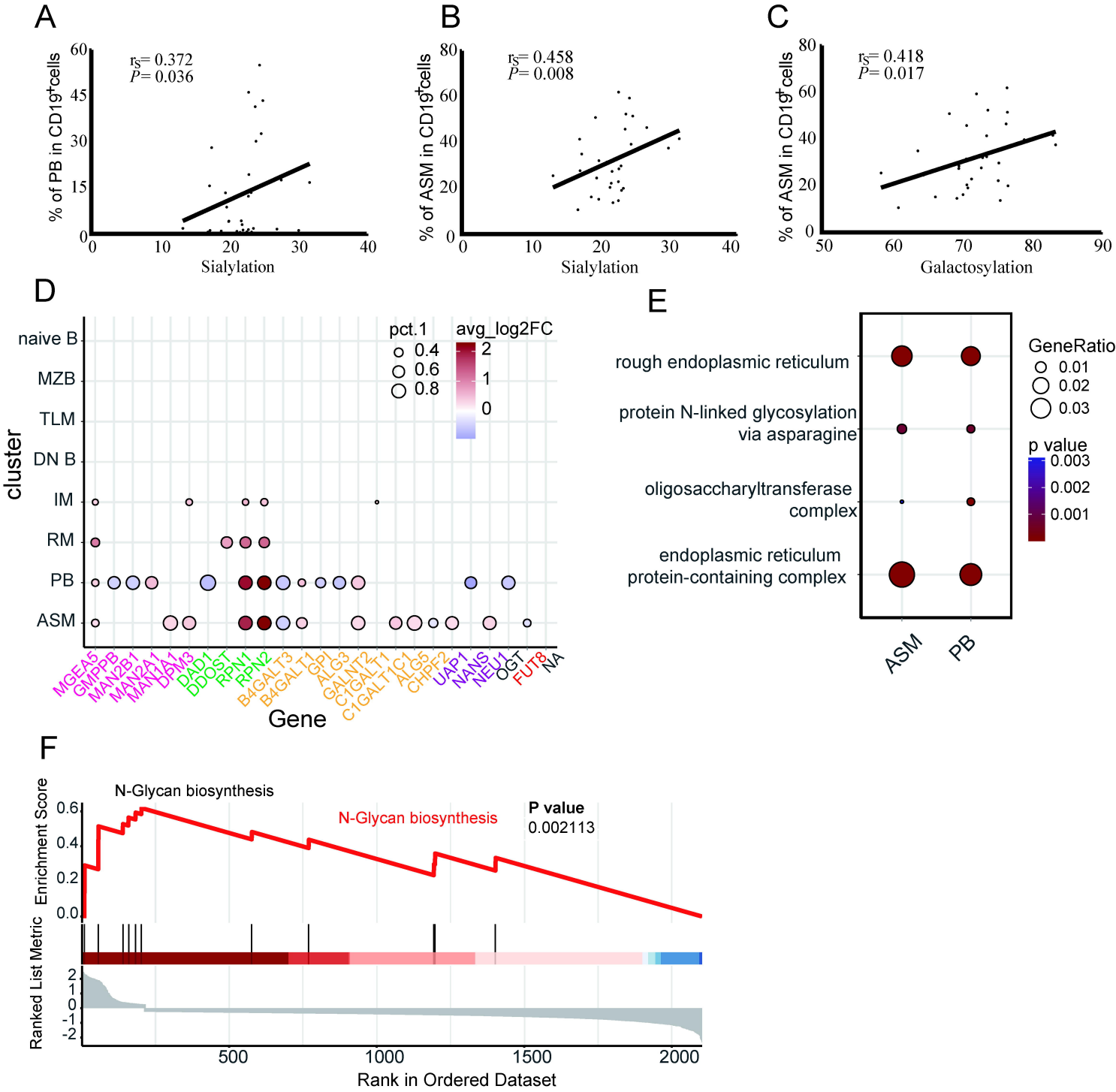
A
% of PB in CD1g+cells
rs= 0.372
P= 0.036
Sialylation
B
% of ASM in CD1g+cells
rs= 0.458
P= 0.008
Sialylation
C
% of ASM in CD1g+cells
rs= 0.418
P= 0.017
Galactosylation
D
naive B
MZB
TLM
DN B
IM
RM
PB
ASM
cluster
pct.1
0.4
0.6
0.8
avg_log2FC
2
1
0
MGEA5
GMPPB
MAN2B1
MAN2A1
MAN1A1
DPM3
PAD1
DDOST
RPN1
RPN2
B4GALT3
B4GALT1
GPI
ALG3
GALNT2
C1GALT1
C1GALT1C1
ALG5
CHPF2
UAP1
NANS
NEU1
OGT
FUT8
NA
Gene
E
rough endoplasmic reticulum
protein N-linked glycosylation via asparagine
oligosaccharyltransferase complex
endoplasmic reticulum protein-containing complex
ASM
PB
GeneRatio
0.01
0.02
0.03
p value
0.003
0.002
0.001
F
N-Glycan biosynthesis
Enrichment Score
N-Glycan biosynthesis
P value
0.002113
Ranked List Metric
Rank in Ordered Dataset

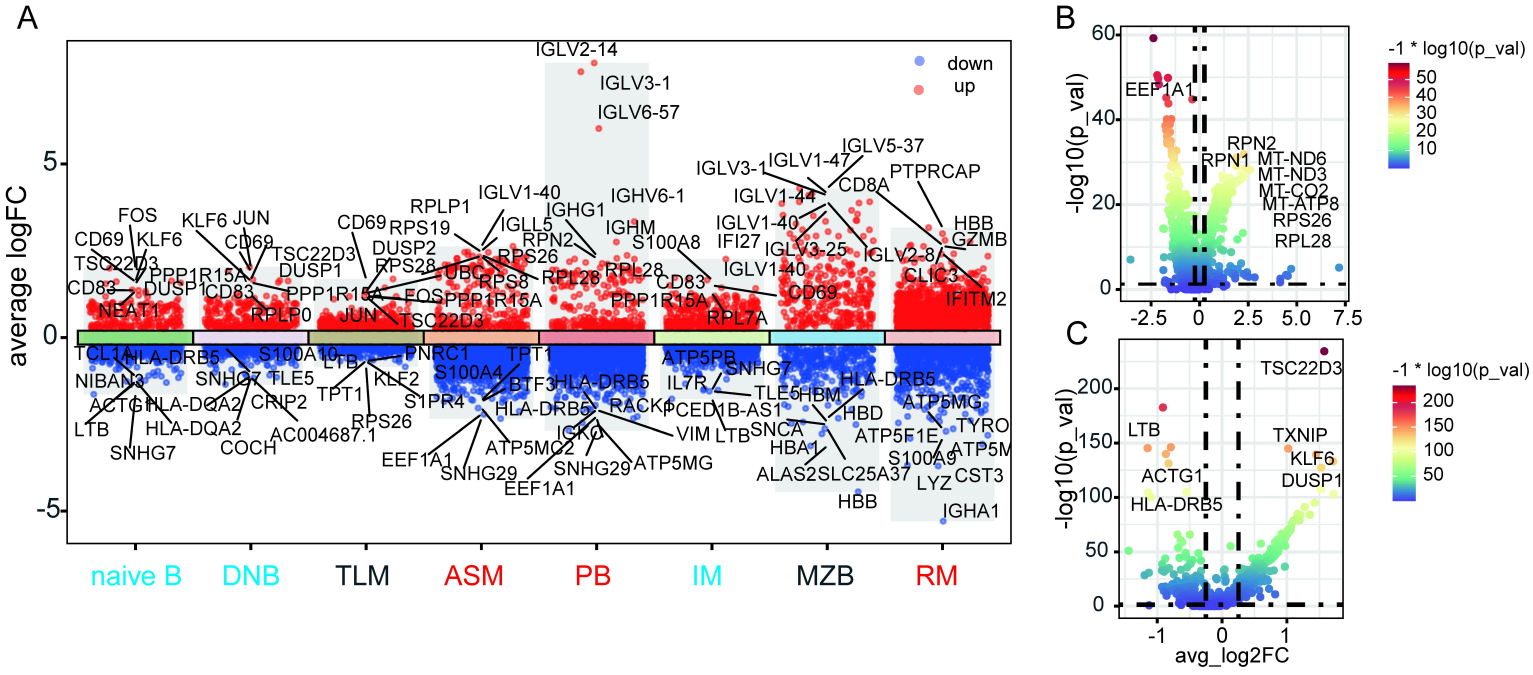
A
average logFC
down
up
naive B
DNB
TLM
ASM
PB
IM
MZB
RM
B
-log10(p_val)
-1 * log10(p_val)
EEF1A1
RPN2
RPN1
MT-ND6
MT-ND3
MT-CO2
MT-ATP8
RPS26
RPL28
C
-log10(p_val)
avg_log2FC
-1 * log10(p_val)
TSC22D3
LTB
TXNIP
KLF6
DUSP1
ACTG1
HLA-DRB5